ELSEVIER

Journal of Nuclear Materials 241–243 (1997) 511–516

journal of nuclear materials

Plasma-surface interactions with ICRF antennas and lower hybrid grills in Tore Supra

J.H. Harris [a,*], T. Hutter [b], J.T. Hogan [a], V. Basiuk [b], B. Beaumont [b], A. Becoulet [b], S. Bremond [b], M.D. Carter [a], M. Goniche [b], R.H. Goulding [a], D. Guilhem [b], G.R. Haste [a], D.J. Hoffman [a], X. Litaudon [b], F. Nguyen [b]

[a] *Oak Ridge National Laboratory, Oak Ridge, TN, USA*

[b] *Centre d'Études de Cadarache, Association EURATOM-CFA sur la Fusion, St. Paul-les-Durance, France*

Abstract

The edge plasma interactions of the actively cooled radio-frequency heating launchers in Tore Supra ion-cyclotron range of frequencies (ICRF) antennas and lower-hybrid (LH) grills are studied using infrared video imaging. On the two-strap ICRF antennas, operated in fast-wave electron heating or current drive mode, hot spots with temperatures of 500–900°C are observed by the end of 2 s power pulses of 2 MW per antenna. The steady-state temperature distribution is determined principally by the relative phase of the two antenna straps: dipole (heating) phasing results in significantly less antenna heating than does 90° (current drive) phasing. Transient heat fluxes of 1–20 MW/m^2 are measured on the lateral protection bumpers at ICRF turn-on; these fluxes are primarily a function of plasma and radio frequency (rf) control. The remarkable feature of the lower hybrid edge interaction is the production of beams of heat flux in front of the grills; these beams propagate along the helical magnetic field lines and can deliver fluxes of 5–10 MW/m^2 over areas of several cm^2 to plasma-facing components. Both the ICRF and LH phenomena appear to result from the acceleration of particles by the near fields of the launchers. Modeling of the heat flux deposition on components and its relation to sputtering processes is presented.

Keywords: TORE SUPRA; boundary plasma; RF heating; sheath physics

1. Introduction

The goal of experiments on the Tore Supra tokamak [1] is to sustain advanced tokamak operation under near steady-state conditions using rf heating. Two rf systems are used: an ICRF system which delivers 5–10 MW through three two-strap antennas and a LH system which delivers 4–6 MW through two wave guide array couplers. The ICRF system is run principally in a fast-wave electron heating (FWEH) mode; the two current straps in each antenna can also be phased for fast-wave current drive (FWCD). The LH system is used for long-pulse current drive. While both systems are capable of delivering power in steady-state, operation is in practice limited by heating of launcher components (most importantly the carbon tiles on the lateral protection bumpers) to temperatures of $\geq$ 1000°C. Once tiles are damaged, the effectiveness of the active cooling is reduced and it is necessary to limit the pulse length.

In Sections 2 and 3 of this paper, we describe detailed IR video imaging studies of edge interactions involving ICRF antennas and LH launchers. In Section 4, we describe modeling of the LH launcher edge interaction that incorporates plasma and surface physics effects and in Section 5, we present conclusions.

2. ICRH antenna interaction experiments

Controlled experiments were done to acquire thermal imaging data [2] on an as yet undamaged ICRF antenna under Tore Supra operating conditions. Two antennas were

* Corresponding author. Tel. : +1-423 574 1180; fax: +1-423 576 7926; e-mail: harrisjh@ornl.gov.

PII S0022-3115(96)00555-7

energized simultaneously: an antenna already in service for some time in port Q1 and a new antenna developed at Oak Ridge National Laboratory (ORNL) and being tested for the first time in port Q5. The new antenna is intended to improve coupling and features a reduced spacing between the current straps and the Faraday screen, a longer effective current strap length and a recessed septum to improve the coupling spectrum for current drive and to improve thermal performance. Both antennas have carbon tile bumpers and Faraday screens coated with B_4C.

The discharge parameters were $B_T = 2.15$ T, $I_p = 0.68$ MA, $q_\psi \approx 4.6$ and $\langle n_e \rangle \approx 3 \times 10^{19}$ m^{-3}. The antennas were energized simultaneously for 2.5 s at $f = 48$ MHz (fast-wave electron heating/current drive mode) and $P_{rf} =$ 2 MW for each antenna. Fig. 1 shows discharge traces for two shots in a sequence. In shot 19708, both antennas were energized with their current straps phased 180° (dipole mode) for FWEH and in shot 19710, the Q5 antenna had its straps phased to 90° for FWCD (co-current drive). In both shots, the antenna-plasma distance dropped from 3–4 cm to 1–2 cm as the rf power rose. The general behavior of the discharge traces for the two shots is similar, although for shot 19710 (Q5 phased for FWCD) there are several dropouts of the ICRF on the Q5 antenna before coupling is established.

The analysis of antenna surface heating presented here focuses on the new ORNL antenna in Q5, because its lateral protection bumpers were still smooth and undamaged, so that the effects of rf power could be separated from those of surface imperfection and projections. Fig. 2 compares IR images and time histories of selected zones on the antenna (4 pixels averaged, resolution ~ 2 cm) for dipole and FWCD operation. The IR images were taken just before rf turn-off at $t \approx 6.5$ s and the framing time of the camera was 0.02 s.

The surface heating patterns for dipole and FWCD phasing show qualitative and quantitative differences. In dipole mode, the regions of strongest heating are the two lateral bumpers, with the hottest regions falling near the equatorial midplane (points a and c on the dipole image in Fig. 2). (There is also a hot region on the lower edge of the antenna box; this was found to be due to a protrusion of the box edge, which was subsequently cut back.) The temperature rises rapidly (~ 0.2 s) and then decreases slightly before becoming approximately constant. This is evidence of a local reduction in heat flux, as the thermal time scale for active cooling of the bumper is 1–2 s, much longer than the time scale of the temperature drop.

In contrast, for FWCD phasing, not only the bumpers but the entire midplane region of the antenna heats up. Additional hot spots appear on the lower corners of the antenna (points d and f in Fig. 2). Many of the hot zones continue to heat throughout the rf pulse. Note that the septum located at the midline of the antenna does not heat because the tubes of the Faraday screen bend away from the plasma by about 2 cm there.

Shots were also taken with the Q5 antenna straps phased at 270°, i.e., counter-current drive. The surface heating pattern is essentially the same as that for 90° phasing. An interesting detail is that the location of the hottest of the lower corner points changes sides, i.e., moves from point f to point d in Fig. 2, when the strap phase is changed from 90° to 270°.

The Q1 antenna shows surface heating patterns qualitatively similar to those seen on the Q5 antenna. The maximum temperatures on the bumpers were higher (800° for dipole operation), but many of the hot tiles showed signs of previous damage — they remained hot for seconds after the rf power turn-off because their contact with the cooling structure had been damaged — so these data are difficult to interpret.

The temperature histories during the initial rise in surface temperature fit $t^{1/2}$ curves, as expected for a solid heating on its inertial time scale. The temperature data can thus be used to calculate an equivalent normal heat flux based on the model of the semi-infinite solid [3]. The heat flux on the contour shown on the right-side bumper of the Q5 antenna during the fast temperature rises in shots 19708 and 19710 is shown in Fig. 3. The calculated fluxes in this case are quite large, with peak values ~ 15–20 MW/m^2, peaked on the equatorial midplane. These fluxes occur for only ~ 0.2–0.3 s, after which the temperature rise slows or ceases (Fig. 2). Studies of other shots with different plasma control details show significantly different fluxes. For example, for another dipole/FWCD comparison (shots 19700 and 19701), the plasma was moved to

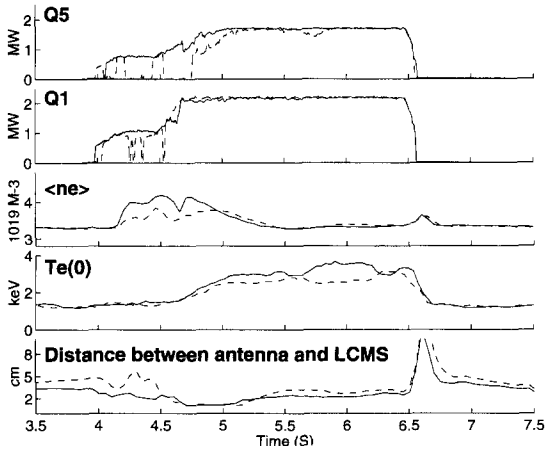

Fig. 1. Diagnostic signals for Tore Supra ICRF heating shots. The solid lines show the signals for shot 19708, for which both the Q1 and Q5 antenna straps were phased at 180° (dipole, FWEH) and the dotted lines show the signals for shot 19710, for which the Q5 antenna straps were phased 90° (FWCD) while the Q1 antenna remained phased at 180°. The top two sets of traces, labeled Q1 and Q5, show the power launched by the respective antennas. The bottommost signals show the distance from the antenna to the last closed magnetic surface (LCMS).

~ 2 cm from the antennas and the rf power was raised slowly to 2 Mw over 1.5 s. In this case, the initial temperature rise is much slower (≈ 1 s) and the calculated fluxes along the right bumper have maxima of 1 MW (dipole) and 3 MW (FWCD). Nevertheless, the surface temperature distributions at the end of the rf pulse are

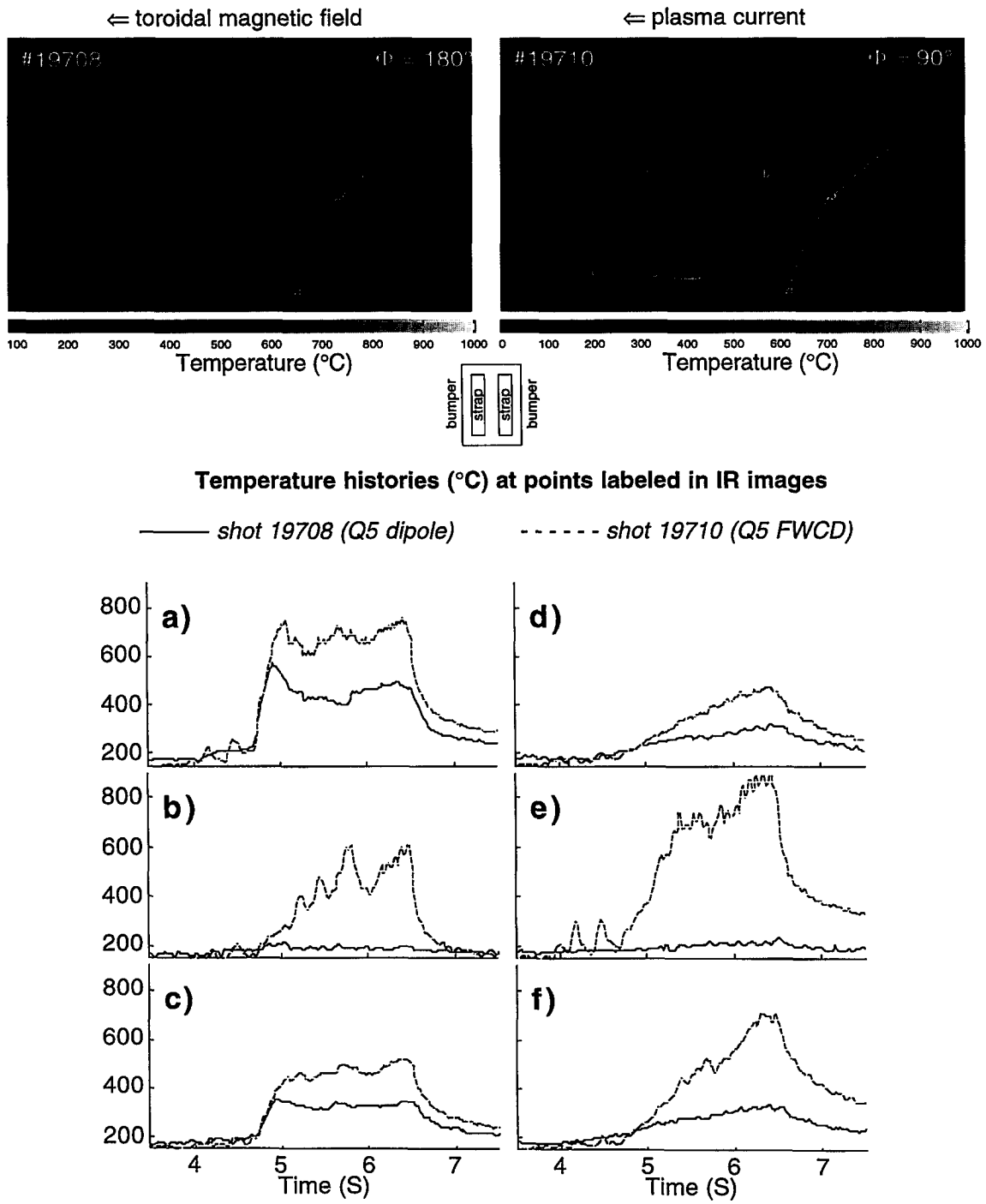

Fig. 2. Infrared images of Q5 (ORNL) antenna for both dipole and FWCD co-current drive strap phasing at end of heating pulse, together with time histories of temperatures for the labeled points in the images. The inset shows a schematic of the antenna, whose image is tilted by the IR optical system. The white lines on the right-hand side bumpers in the IR images indicate the contours for the heat flux profiles shown in Fig. 3.

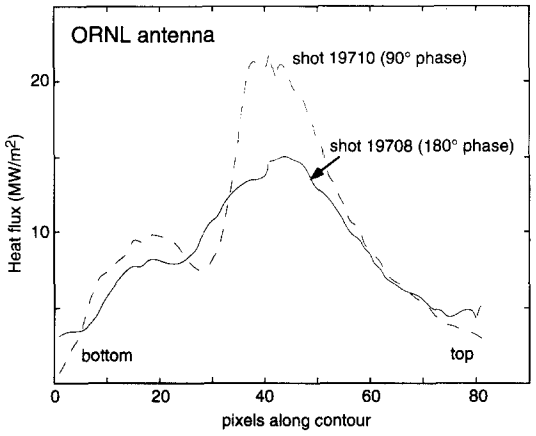

Fig. 3. Heat flux profile on lateral protection bumper contours shown in Fig. 2. Measurements made during period of fast surface temperature rise, 4.7–5.0 s.

essentially the same as for the respective cases shown in Fig. 2. Thus, while operational details may determine the transient heat flux that falls on the antenna at rf power-on, the steady-state heating pattern is primarily determined by the geometric structure of the rf field in front of the antenna.

Laboratory measurements with a directional detector of the poloidal rf electric field — the principal drive launched by the current strap — in front of the unloaded antenna (Fig. 4) show the essential difference between dipole and FWCD operation. The dipole configuration has a field null on the antenna septum where the field changes sign, while the FWCD configuration has only a slight dip. Vertical scans of the poloidal component show that it has a broad maximum on the equatorial midplane. Measurements of the field component normal to the antenna face show higher maxima at the top and bottom of the antenna for FWCD phasing. Detailed modeling of the field structure in the presence of plasma loading is being carried out using a modified version of the RANT-3D code [4].

These results suggest that the pattern of antenna surface

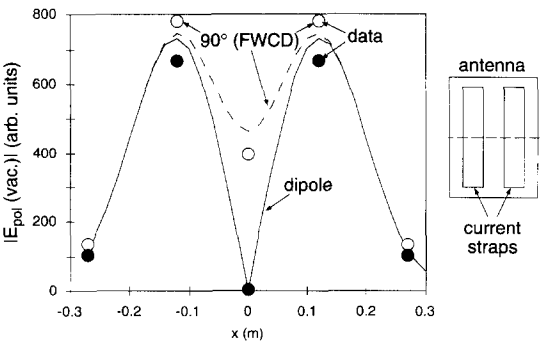

Fig. 4. Rf poloidal electric field measured 1 cm in front of Faraday screen of ORNL antenna. In the dipole configuration, there is a null in the field magnitude on the center line.

heating is related to the rf field directly in front of the antenna and presumably the resultant particle acceleration and charge flows. Dipole phasing reduces the antenna heating by reducing the rf field near the antenna. If we apply a sheath rectification analogy [5] and use effective potential values of 1–10 kV, comparable to the rf potentials in front of the antenna, the current densities required to produce the measured power fluxes are 100–1000 A/m^2.

3. LH coupler interaction experiments

Previous studies [2] of the interactions of the LH couplers with the edge plasma showed that beams of heat flux emanate along the centerline of each wave guide row and impinge upon the bumpers on both sides of the grill, leading to significant temperature rises of 400°C or more. Calculations of local electron acceleration directly in front of the grill showed that the electron distribution function broadens, with tail energies in the range of 3–5 keV and mean electron energies of 300–500 eV. Such populations can lead to the heating observed on the lateral bumpers of the LH launcher (Section 4).

Recent experiments have shown that the beams of heat flux pass beyond the bumpers and follow the magnetic field lines, where they can strike other plasma-facing components. By adjusting the plasma current (and hence the edge safety factor $q(a)$) it is possible to place the beams on particular components whose response can be monitored using the IR imaging system. By choosing $q(a)$ so that the LH couplers are magnetically connected to a vertical limiter and then varying $q(a)$ slightly and firing the two couplers in succession, it has been possible to identify the hot spots that result from each of the four rows of wave guides in the two couplers. The total power carried in these beams is small, $\lesssim 1\%$ of the LH power launched by the couplers, but locally elevated fluxes can cause damage to plasma facing components.

An extreme example of the effect of the LH-produced heat fluxes on another component — an ICRF antenna — is shown in Fig. 5. In this case, magnetic field lines connect the grill with the lateral bumper of the antenna and the LH coupler is placed ~ 8 cm further away from the plasma than the ICRF antenna. The LH coupling is reduced (which increases the accelerating LH electric field) and the heat flux tubes strike squarely on the side of the ICRF antenna bumper. The heat flux estimation technique described in Section 2 produces the profile of heat flux along the bumper shown in Fig. 5. The peak values of ~ 8 MW/m^2 shown reflect an average over zones of size ~ 1 cm.

4. Modeling of the LH surface interaction

An evaluation of the mechanisms involved in the interaction of the LH-accelerated electrons with the lateral

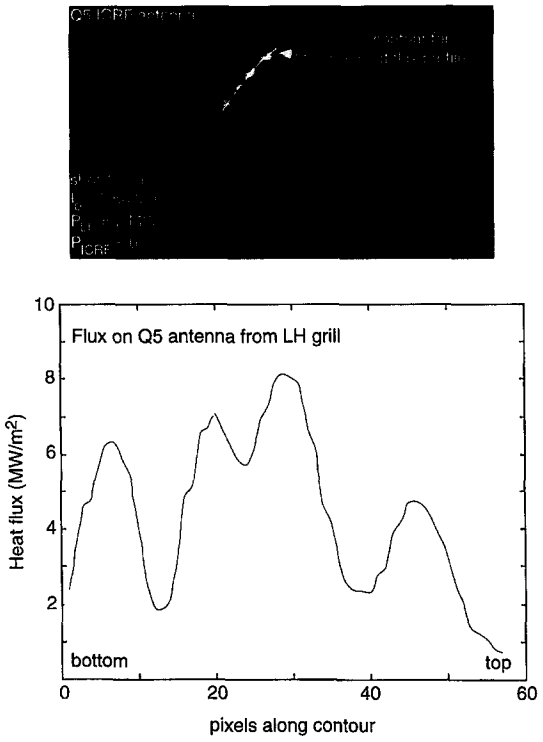

Fig. 5. Infrared image of unpowered ICRF antenna during LH heating, with LH grill magnetically connected to ICRF lateral protection limiters, together with measured heat flux profile along the contour shown. The hot spots reach 800°C in approximately 1 s.

bumpers on the grill or the ICRF antenna has been carried out using the BBQ impurity SOL transport code and the CASTEM-2000 finite element thermal analysis code. The input SOL parameters for modeling are based on reciprocating Langmuir probe profiles for similar discharges. Because the incident heat flux to the surface of the lateral protection depends on the instantaneous temperature of the surface and this surface is actively cooled, a self-consistent thermal analysis is required, including the instantaneous local sheath potential. Fast electron, thermionic emission and secondary electron emission effects on the sheath potential have thus been included in CASTEM. The heat flux conducted away from the wall is calculated by CASTEM and includes contributions due to bulk conduction, thermal radiation, evaporative and thermionic cooling. The model calculates the condition of zero net electron current to the surface, including the effects of secondary electron and ion emission. The heat flux from the plasma to the wall is then computed. A heat flux enhancement due to a fast-electron minority with average energy ~ 10 times the background T_e is included, using the model described in Ref. [6]. In front of the Tore Supra LH couplers, the fast electron population is $\sim 10\%$ of the bulk population.

This calculation predicts a substantial increase in the heat flux transmitted through the sheath, due to a decrease in the sheath potential, which results in direct fast electron heating. The analysis of the allowable operating regime consists of evaluating the particle balance for two species ('high' and 'low' energy) of C impurities, as described in Ref. [7]. Physical sputtering produces a Thomson distribution of particles with higher energies (> 1 eV), whereas processes such as chemical sputtering and radiation-enhanced sublimation (RES) produce thermal particles with lower energy (~ 0.1 eV). The latter are more likely to be ionized close to the surface (within the magnetic Debye sheath) and redeposited on the surface without being accelerated by the sheath, while the former may be redeposited at the surface with energy $\sim 3kT_e$. The total flux of C atoms with 'high' energy is thus the sum of fluxes of the physically sputtered particles and those produced by sputtering due to the redeposited fluxes.

Additional terms have been added in to those in the original analysis [7] to include low energy chemical sputtering self-consistently and to include the low energy particles produced by evaporation at high temperatures, where thermionic emission effects are important. The revised low energy particle balance thus introduces chemical, RES and thermionic effects. The basic data used in this model are the physical, chemical and RES sputtering yields, updated [8] to account for the 'athermal' mechanism which produces chemical sputtering at lower temperatures than have been previously considered. The impurity runaway condition determines the limit to the predicted allowable operating space. The analysis has been updated by including: (1) the localized redeposited heat flux due to C impurities and increased physical sputtering coefficients for D incident on C; (2) the dependence of the incident

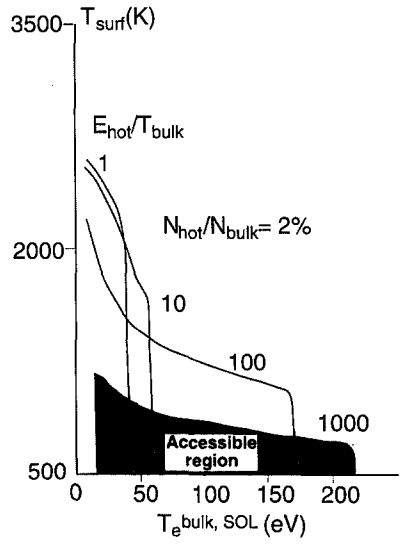

Fig. 6. Operating space for carbon plasma facing component (e.g., lateral protection bumper of LH coupler) subjected to fast electron as well as thermal plasma fluxes.

heat flux on the secondary electron emission (SEE) coefficient and (3) including the effects of the LH fast electrons on the sheath potential. The resulting operational space for cases with $n_{hot}/n_{bulk} = 2\%$ and $T_{hot}/T_{bulk} = 1-1000$, is shown in Fig. 6.

The operational space with inclusion of fast electron effects may be limited to $T_e(SOL) < 60$ eV and maximum surface temperatures $T_{surf} < 1500-2500$ K. The Tore Supra LH lateral protection is actively cooled, so that under normal conditions, such a high surface temperature would not be attained. However, localized overheating is still possible and the production of localized heat fluxes due to redeposition of impurities and fast electron sheath effects could produce the observed local spots. CASTEM was used to examine local impurity production and it was found that localized chemical production can occur as T approaches 1000°K.

5. Discussion

The launching of rf power into the tokamak edge plasma can result in substantial heat fluxes to the rf launchers themselves and to other components connected to them by the helical magnetic field lines. Some reduction of the fluxes can be effected by optimizing the rf field configuration of the launcher so as to minimize stray rf components, as is shown with dipole phasing of the ICRF antenna straps. Antenna design changes to improve coupling may also help reduce particle acceleration in the plasma edge. Measurements of the energy of the accelerated particles would help in improving the modeling of these effects.

Mitigation of the effects of the fluxes on other components involves control of the magnetic connections. Sweeping the radial position of the launcher or a small time-variation of $q(a)$ may reduce the heat flux to connected components. Improved bumper designs (larger sloping surfaces, more efficient cooling) and material coatings (e.g., B_4C) that reduce impurity production can improve component performance. Efforts in all these areas are underway for Tore Supra.

Acknowledgements

This work was supported in part by the Office of Fusion Energy, U.S. Department of Energy, under contract DE-AC05-96OR22464 with Lockheed–Martin Energy Research Corporation.

References

[1] Equipe Tore Supra, Plasma Phys. Contr. Nucl. Fusion 36, (1994) B123.
[2] J.H. Harris et al., eds., Proc. 22nd European Physical Society Conference on Controlled Fusion and Plasma Physics, Part IV (1995) p. 397.
[3] H.S. Carslaw and J.C. Jaeger, Conduction of Heat in Solids (Oxford University Press, 1984).
[4] M.D. Carter et al., Nucl. Fusion 36 (1996) 209.
[5] J.-M. Noterdaeme and G. Van Oost, Plasma Phys. Contr. Nucl. Fusion 35 (1993) 1481.
[6] K. Sato and F. Iwasaki, Natl. Inst. Fusion Sci. Rept. NIFS-136 (1992).
[7] J.N. Brooks, J. Nucl. Mater. 170 (1990) 164.
[8] C. Garcia-Rosales and J. Roth, Proc. 21nd European Physical Society Conference on Controlled Fusion and Plasma Physics, Part II (1994) p. 397.